batteries

MDPI

Article

Earth-Abundant Titanium Dioxide-Mesoporous Carbon as a Dual-Confinement Host for Lithium–Sulfur Batteries

Jeonghwan Song, Jinju Song * and Il-Chan Jang *

Gwangju Clean Energy Research Center, Korea Institute of Energy Research (KIER), Gwangju 61003, Republic of Korea; song5371@kier.re.kr

* Correspondence: jinju@kier.re.kr (J.S.); jic7421@kier.re.kr (I.-C.J.)

Abstract

Lithium–sulfur (Li-S) batteries are attractive next-generation energy storage systems owing to their high theoretical energy density of 2600 Wh/kg and earth-abundant, eco-friendly sulfur. However, their practical application is hindered by the insulating nature of sulfur, large volume changes during cycling, and the polysulfide shuttle effect. Herein, we designed a dual-confinement cathode architecture combining mesoporous carbon with earth-abundant titanium dioxide (TiO_2). Sulfur composites with 70 wt% sulfur loading were prepared. Structural characterization via X-ray diffraction (XRD) and Brunauer–Emmett–Teller (BET) analysis showed a well-developed mesoporous network in KB but not in TiO_2. XRD confirmed that sulfur and anatase TiO_2 coexist in the composites, with weaker sulfur peaks in the mixed host. UV-vis absorption spectra showed that nano-TiO_2 removes more Li_2S_6 from solution than KB. Electrochemical evaluations revealed that the dual-confinement composite architecture balances the fast redox kinetics of carbon against the polysulfide affinity of TiO_2. Consequently, the composite achieved a high initial discharge capacity of 1300.89 mAh/g at 0.1 C and stable cycling over 100 cycles at 0.5 C. Furthermore, ex situ XRD analysis revealed nearly complete sulfur conversion while maintaining TiO_2 structural integrity. These results demonstrate an optimal balance between electronic conductivity and polysulfide mitigation via a sustainable material strategy.

Keywords: Lithium–sulfur battery; shuttle effect; Ketjen black; titanium dioxide; dual-confinement; earth-abundant

1. Introduction

Rapidly growing demand for electric vehicles (EVs) and large-scale energy storage systems (ESS) has increased the need to develop next-generation batteries with energy densities surpassing those of conventional lithium-ion batteries (LIBs, ~250 Wh/kg) [1,2]. Although LIB technologies have achieved remarkable milestones, the commercial cathode materials have limited theoretical capacity (e.g., ~274 mAh/g for $LiCoO_2$, with a practical value of ~140 mAh/g), while relying heavily on critical, scarce transition metals (e.g., Co, Ni) with severe supply chain risks, thereby imposing a fundamental bottleneck on high-energy density storage devices [3,4]. According to proactive projections by the International Energy Agency (IEA), the global EV market is anticipated to expand at a compound annual growth rate exceeding 25% through 2030 [5], highlighting the urgency of developing post-LIB technologies with two- to three-fold higher energy densities and sustainable resource availability. To accommodate these rigorous requirements, a multitude of promising next-generation battery systems have been proposed. Among the various

Check for updates

Academic Editor: Jianqing Zhao

Received: 13 August 2026
Revised: 13 September 2026
Accepted: 21 September 2026
Published: 22 September 2026

Copyright: © 2026 by the authors. Licensee MDPI, Basel, Switzerland. This article is an open access article distributed under the terms and conditions of the Creative Commons Attribution (CC BY) license.

candidates, including lithium–air and all-solid-state batteries, lithium–sulfur (Li-S) batteries offer distinct advantages owing to their exceptionally high theoretical energy density of 2600 Wh/kg and the high theoretical specific capacity of sulfur (1675 mAh/g) [6–8]. Crucially, sulfur is highly attractive from both economic and environmental perspectives, given that it is the earth-abundant element (the 16th most abundant in the Earth's crust), costs approximately 0.1 $/kg, and is environmentally benign [9,10].

Despite these advantages, the commercial viability of Li-S batteries is hindered by three critical challenges. First, the highly insulating nature of both elemental sulfur (S_8, $\sigma_{S8} \approx 5 \times 10^{-30}$ S/cm) and the final discharge products (Li_2S, Li_2S_2, $\sigma_{Li2S} \approx 10^{-13}$ S/cm) critically restricts charge transport, leading to poor sulfur utilization [11,12]. Second, the ~80% volume expansion during the S_8-to-Li_2S conversion (ρ_{S8} = 2.07 g/cm^3 → ρ_{Li2S} = 1.66 g/cm^3) causes repeated mechanical stress on the electrode, which deteriorates structural integrity and increases contact resistance [13,14]. Third, and most critically, the intermediate long-chain lithium polysulfides (Li_2S_n, $4 \leq n \leq 8$) readily dissolve into ether-based electrolytes and shuttle between the cathode and anode [15,16]. This polysulfide shuttle leads to severe active material degradation, low coulombic efficiency (<90%), continuous anode passivation, and uncontrollable dendrite growth, all of which drastically undermine both long-term cyclability and device safety [17,18].

To address these issues, various porous carbon frameworks such as Ketjen black (KB), carbon nanotubes, graphene, ordered mesoporous carbon, and activated carbon have been widely explored to physically encapsulate sulfur species [19–22]. Among these candidates, KB offers particular architectural advantages due to its high specific surface area and well-developed mesoporous network, which facilitate high sulfur loading and establish continuous electron conduction pathways [23,24]. Since the pioneering work of Ji et al. [19], porous carbon–sulfur composites have served as the mainstream cathode design for Li-S batteries. Nevertheless, the nonpolar carbon surface interacts only weakly with polar lithium polysulfides through van der Waals forces, making it difficult to suppress the progressive leaching of polysulfides into the electrolyte during cycling [25,26]. This critical drawback was recently highlighted by Nizami et al., who confirmed that even porosity-optimized Black Pearl carbon hosts lack the chemical anchoring capability required to guarantee long-term polysulfide immobilization [27].

To overcome these limitations of carbon hosts, the integration of polar compounds—such as transition metal oxides, sulfides, and nitrides—has been actively pursued to chemically immobilize polysulfides and promote their redox conversion [28–31]. Among these, titanium dioxide (TiO_2) has emerged as a particularly promising anchoring material owing to its cost-effectiveness, exceptional earth abundance (titanium being the 9th most abundant element in the Earth's crust), and non-toxicity. Mechanistically, the surface Ti^{4+} sites of TiO_2 form strong Lewis acid–base coordination with the terminal S^{2-} anions of polysulfides [28,32,33]. For instance, Seh et al. showed that yolk–shell TiO_2–S nanostructures exhibit a strong chemical affinity for polysulfide species, which greatly mitigates capacity fading compared to bare sulfur cathodes [28]. Similarly, Tao et al. also confirmed that incorporating TiO_2 on graphene frameworks can trap polysulfides and retain them near the conductive carbon surface [32]. However, TiO_2 is a wide-bandgap semiconductor (~3.2 eV for anatase) with very low electronic conductivity ($\sigma \approx 10^{-12}$ S/cm), which imposes a critical bottleneck on charge transport when used as a standalone host [34]. Therefore, combining KB and TiO_2 at an optimized ratio can achieve a dual-confinement effect: the physical entrapment and electron transport network of KB with the chemical polysulfide anchoring of the earth-abundant TiO_2.

In this work, we investigate the influence of the conductive carbon-to-polar oxide ratio on the electrochemical performance of Li-S batteries by fabricating S/KB/TiO_2 compos-

ites via an autoclave-based melt-diffusion method. Four compositions were examined: a carbon-only host (S:KB = 7:3, SK73), an oxide-only host (S:TiO_2 = 7:3, ST73), and two dual-confinement hosts (S:KB:TiO_2 = 7:1:2, SKT712; = 7:2:1, SKT721). Physical characterization (thermogravimetric analysis (TGA), X-ray diffraction (XRD), Brunauer–Emmett–Teller (BET), scanning electron microscopy (SEM)) and electrochemical evaluation (CV, galvanostatic cycling) were performed to clarify the structure–performance relationships. KB–TiO_2 hybrid hosts and the complementary roles of their components are well established. The contribution of the present work is not a new host chemistry but a controlled compositional series in which the conductive-carbon-to-polar-oxide ratio is varied across its full range while the synthesis route, sulfur content and electrode fabrication are held constant, allowing the resulting trade-off between charge-transport kinetics and capacity retention to be traced and an optimum to be located within that range. Consequently, this work presents a simple, scalable, and resource-sustainable composition-optimization guideline to accelerate the rational design of earth-abundant Li-S cathodes (Figure 1).

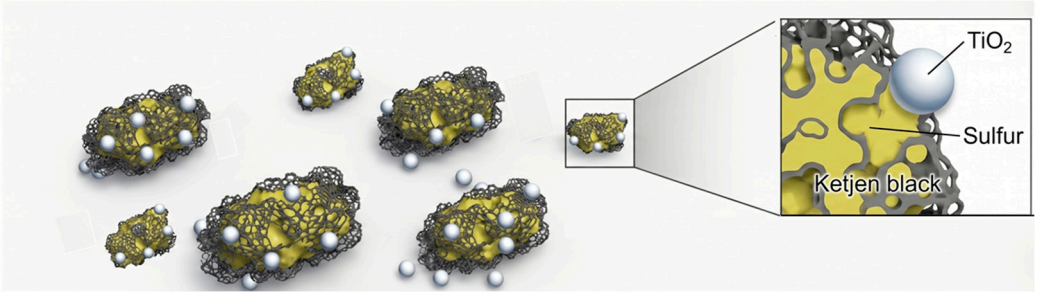


Figure 1. Schematic diagram of the dual-confinement strategy in S/KB/TiO_2 composite cathodes.

2. Materials and Methods

2.1. Materials

Mesoporous carbon (Ketjen Black, KB; Nouryon 600JD, Nouryon, Amsterdam, The Netherlands), sulfur (Sigma-Aldrich, St. Louis, MO, USA), and synthesized nano-TiO_2 were used to prepare the cathode composites.

2.2. Synthesis of Nano-TiO_2

Nano-TiO_2 was prepared following a previously reported procedure with the same precursor ratio. Briefly, lepidocrocite-type $Cs_{0.67}Ti_{1.83}O_4$ was reacted in a solution with a TBA^+/H^+ molar ratio of 1 for 3 days to yield a stable colloidal suspension. Subsequently, the as-prepared TiO_2 colloid was dried in a convection oven at 60 °C for 3 days to obtain the precursor powder.

2.3. Preparation of Sulfur Composites

Four composites were prepared using sulfur, KB, and/or nano-TiO_2: S:KB = 7:3 (SK73), S:TiO_2 = 7:3 (ST73), S:KB:TiO_2 = 7:2:1 (SKT721), and S:KB:TiO_2 = 7:1:2 (SKT712) (weight ratio). The precursor mixture was loaded into a Teflon-lined autoclave with N-methyl-2-pyrrolidone (NMP) (solid:NMP = 1:3, *w*/*w*) and heated at 180 °C for 6 h. After cooling, the products were collected and dried.

2.4. Preparation of Li_2S_6 Solution

Sulfur (Sigma Aldrich, St. Louis, MO, USA) and Li_2S (Sigma Aldrich, St. Louis, MO, USA) were added to 1,3-dioxolane/1,2-dimethoxyethane (DOL/DME; *v*/*v* = 1/1). Afterward, the solution was heated to 60 °C and stirred for 24 h under an argon atmosphere to yield the Li_2S_6 solution.

2.5. Electrochemical Measurements

Cathode slurries were prepared by mixing active material (composite), conductive additive (Super P), and binder (polyvinylidene fluoride, PVDF) in a weight ratio of 7:2:1 in NMP. The slurry was coated on aluminum foil and dried to form the cathode. CR2032 coin cells were assembled in an Ar-filled glovebox using the composite cathode (14 mm diameter) and a lithium-metal anode (16 mm diameter). The electrolyte was 1 M lithium bis(trifluoromethanesulfonyl)imide (LiTFSI) in DOL/DME (v/v = 1/1), with 160 µL added per cell. Galvanostatic charge/discharge tests were conducted between 1.7 and 2.8 V at 0.1 C and 0.5 C. Rate capability was evaluated at 0.1, 0.2, 0.5, 1.0 and 2.0 C, with five cycles at each step, followed by a return to 0.5 C. The cathode was 14 mm in diameter (1.54 cm^2), with a sulfur areal loading of 1.36–1.47 mg cm^{-2}, corresponding to 2.09–2.26 mg of sulfur per cell. Sulfur accounted for 49 wt% of the electrode (70 wt% composite × 70 wt% sulfur). With 160 µL of electrolyte per cell, the electrolyte-to-sulfur (E/S) ratio was 71–77 µL/mg.

2.6. Characterizations

The electrode composition was determined by TGA (Mettler Toledo TGA2, Mettler Toledo, Greifensee, Switzerland) in air at a heating rate of 10 °C min^{-1}, from 30 °C to 500 °C.

Brunauer–Emmett–Teller (BET) for pore size of materials was Belsorp MAX-II (MicrotracBEL Corp., Osaka, Japan), pretreatment was 200 °C, 12 h under the vacuum, and nitrogen adsorption–desorption isotherms were subsequently measured.

UV-Vis absorption spectra were collected using UV grade quartz cuvette having a light path of 0.2 mm (Shimadzu, Japan).

X-ray diffraction (XRD) patterns of powder and electrode samples were recorded on a Rigaku (Tokyo, Japan) SmartLab diffractometer using Ni-filtered Cu $K\alpha_1$ radiation (λ = 1.54059 Å) at 40 kV and 44 mA, with a 2θ range of 10–80° in 0.2° steps.

Morphology was examined by table scanning electron microscopy (table SEM; Sec SNE-4500M, SEC Co., Ltd., Suwon, Republic of Korea).

Electrochemical measurements were conducted using a WonAtech battery cycler (2PD-CCJ16, WonATech Co., Ltd., Seoul, Republic of Korea) and EC lab-Biologic SP-300 (BioLogic, Seyssinet-Pariset, France).

3. Results and Discussion

The characteristically low melting temperature of sulfur facilitates the fabrication of S/KB/TiO_2 composites under moderate thermal operations. To gain initial structural insights, the surface morphologies of the precursor materials were first examined by SEM (Figure 2). While bulk sulfur possesses a micrometer-scale particle morphology, both KB (Figure 2b) and TiO_2 (Figure 2c) show nano-particulate structures consisting of agglomerated clusters with dimensions in a range of tens of nanometers. Consequently, these nanosized host components are expected to readily encapsulate the melted sulfur, ensuring the successful formation of well-dispersed S/KB/TiO_2 composites.

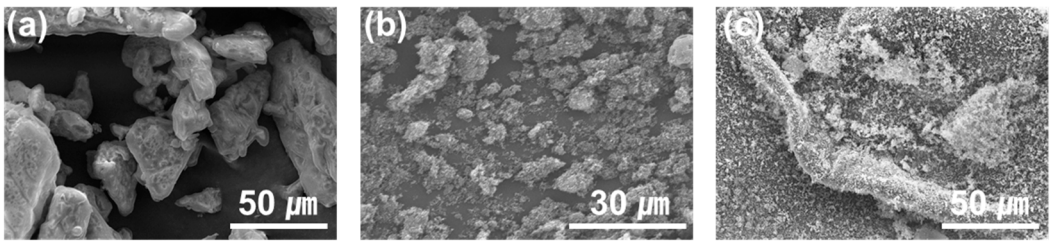


Figure 2. SEM images of raw materials: (**a**) sulfur, (**b**) Ketjen Black, (**c**) TiO_2.

The pore structures of KB and TiO_2 were evaluated by BET N2 adsorption–desorption analysis, as illustrated in Figure 3. The isotherm profile of KB showed a typical Type IV characteristic with a pronounced hysteresis loop in the relative pressure range at P/P0 = 0.4–0.9. This behavior firmly validates the presence of a well-developed mesoporous network (2–50 nm), which is highly advantageous for driving homogeneous sulfur infiltration, facilitating efficient electrolyte penetration, and buffering the severe structural volume-change during extended cycling. In contrast, TiO_2 exhibited a low N_2 adsorption volume, followed by a pronounced increase in adsorption at high relative pressures. Following IUPAC guidance, this profile indicates that accessible pore volume arises mainly from relatively large interparticle voids rather than intraparticle porosity [35], consistent with the agglomeration of TiO_2 nanoparticles observed in the SEM image (Figure 2c) [36]. KB had a BET surface area of 483.6 m^2/g, a total pore volume of 0.3782 cm^3/g, and a mean pore diameter of 3.13 nm, while TiO_2 had 93.2 m^2/g, 0.2795 cm^3/g, and 12.00 nm. The high surface area and small pores of KB reflect its mesoporous network, whereas the low surface area and larger mean pore size of TiO_2 indicate that its pore volume comes mainly from voids between particles. This fundamental structural difference reflects the distinct roles of the two constituents within Li-S cells: KB acts as a highly conductive framework and a primary physical sulfur host, whereas TiO_2 functions effectively as a localized chemical polysulfide immobilizer.

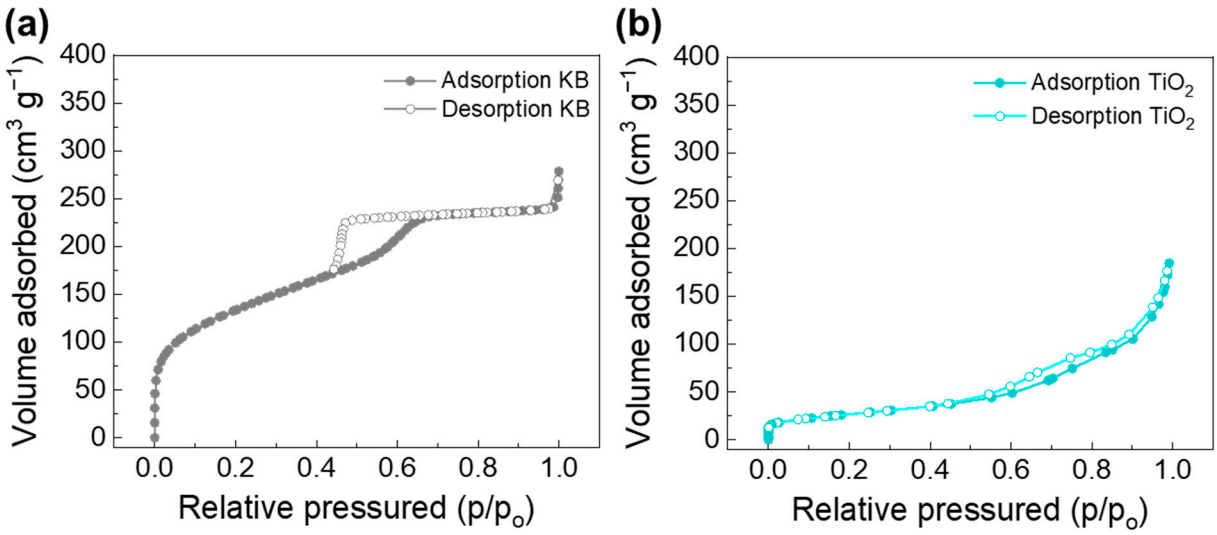


Figure 3. N_2 adsorption–desorption isotherm results: (**a**) KB, (**b**) TiO_2.

To test the second of these roles directly, a static adsorption experiment was carried out on the two host components. Equal masses of KB and nano-TiO_2 were immersed in a Li_2S_6 solution for 4 h together with an identically treated blank, and the supernatants were compared by UV-vis spectroscopy (Figure 4). The blank shows the absorption bands characteristic of long-chain polysulfide anions below approximately 350 nm. After contact with KB, these bands are only slightly reduced, whereas after contact with nano-TiO_2 they fall markedly, and the inset photographs show the corresponding loss of color in the TiO_2 vial. The two components were compared at equal mass, and the BET surface area of TiO_2 (93.2 $m^2\ g^{-1}$) is roughly one fifth that of KB (483.6 $m^2\ g^{-1}$), so the larger uptake by the oxide cannot be attributed to a larger contact area. It indicates instead an interaction that the polar oxide surface provides and the nonpolar carbon surface does not, consistent with the Lewis acid–base coordination between surface Ti^{4+} sites and terminal S^{2-} anions reported for TiO_2 hosts [28,32]. The measurement establishes the relative affinity of the two host

surfaces for dissolved polysulfides under static conditions; it does not by itself demonstrate that the same interaction governs the behavior of the cycled composite electrodes.

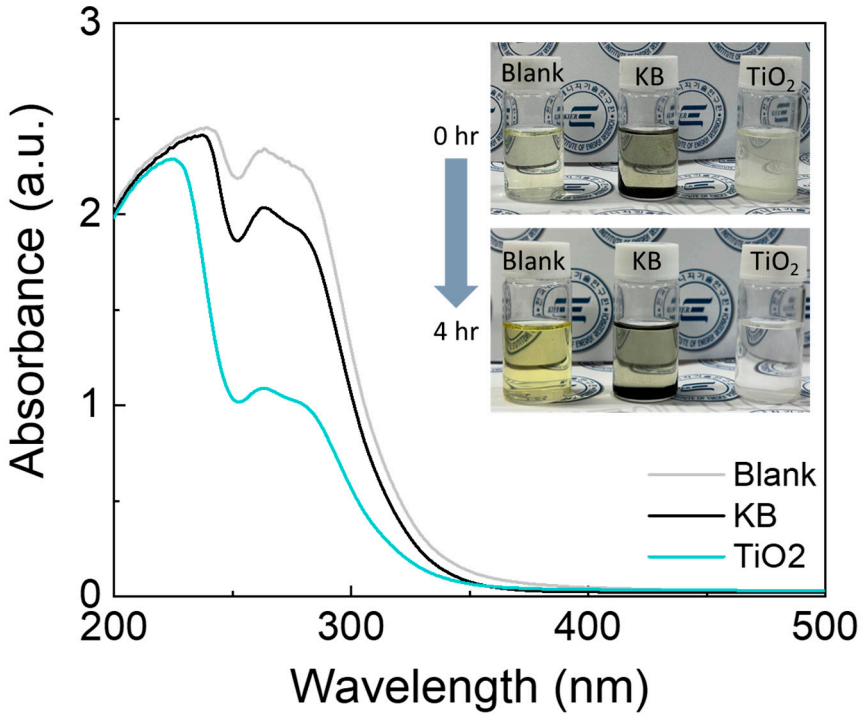


Figure 4. UV-vis adsorption spectra of Li_2S_6 solution on KB and TiO_2; inset: photos of Li_2S_6 solution before and after anchoring for 4 h (background: KIER logo in Korean and English).

Thermogravimetric analysis (TGA) confirmed that all four composites (SK73, ST73, SKT712, SKT721) successfully achieved a targeted sulfur loading of approximately 70 wt%, as shown in Figure 5. The initial thermal weight loss began near 200 °C due to the volatilization of sulfur and reached completion at near ~350 °C, yielding a persistent residual mass of approximately ~30% for all examined samples, which precisely aligns with the target compositions. This consistent thermochemical profile substantiates that the autoclave assisted process (180 °C, 6 h) achieves uniform and reproducible sulfur infiltration, irrespective of the underlying host framework. This rigorous compositional control ensures that any variations in electrochemical performance can be decoupled from mass loading effects and attributed solely to the intrinsic physicochemical properties of the respective host matrices.

Scanning electron microscopy (SEM) analysis revealed distinctive morphologies for each composite, as illustrated in Figure 6. The SK73 exhibited a highly interconnected porous KB network within which sulfur was effectively infiltrated. Conversely, the ST73 showed relatively large TiO_2 agglomerates driven by the high surface energy inherent to the nanoparticles, which can hinder uniform charge distribution during cycling. In case of SKT712, a non-uniform distribution characterized by localized TiO_2 aggregates was observed, which is ascribed to its elevated TiO_2 content. In contrast, SKT721 showed no comparable TiO_2 aggregates, indicating a more even distribution of the oxide across the KB matrix. In SKT712, the excessive TiO_2 content not only produced this aggregation but also reduced the available internal pore volume. These observations are limited to the micrometer scale accessible with the table-top SEM used here; the distribution of TiO_2 within the KB matrix at the nanoscale was not verified.

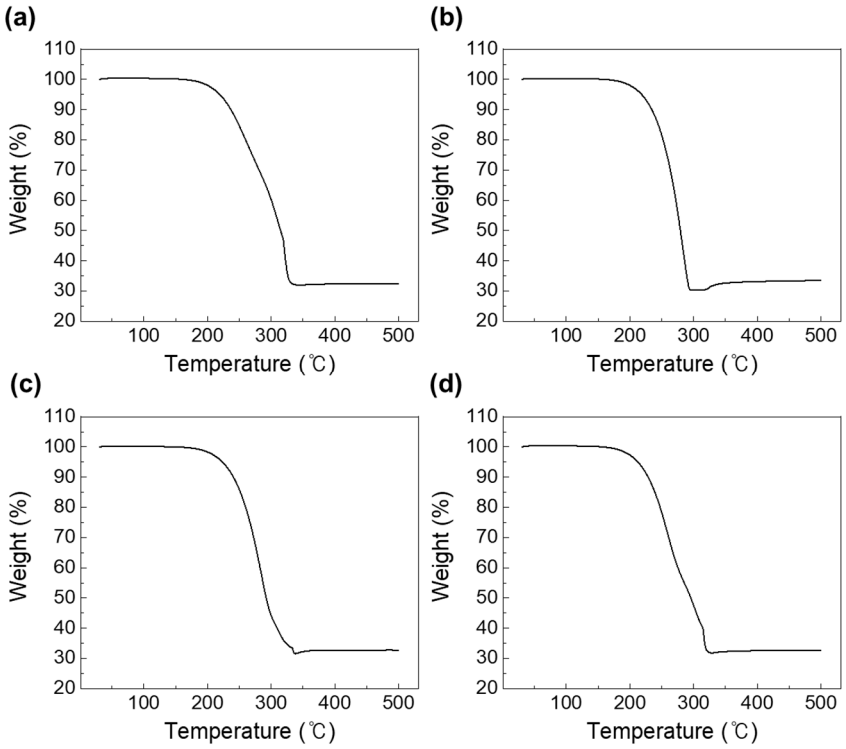


Figure 5. TGA results: (**a**) SK73, (**b**) ST73, (**c**) SKT712, (**d**) SKT721.

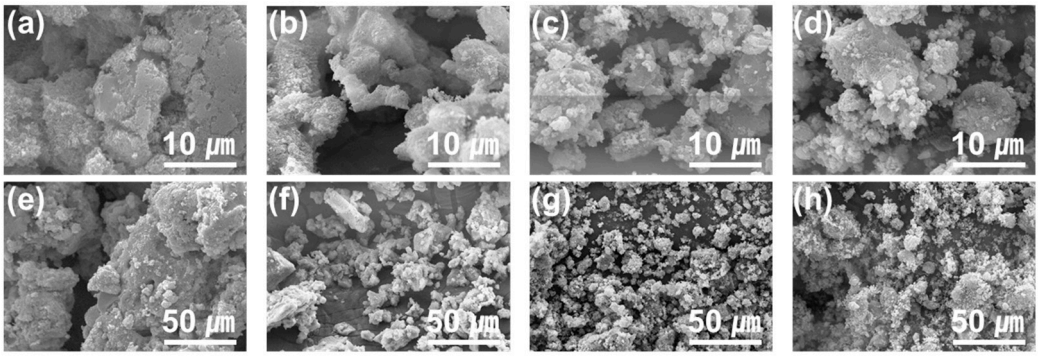


Figure 6. SEM images of composites: (**a**,**e**) SK73, (**b**,**f**) ST73, (**c**,**g**) SKT712, (**d**,**h**) SKT721.

SKT721 combines these two properties through three working mechanisms. First, KB serves as the major framework of the host (two-thirds of the host by weight), providing a continuous electron pathway throughout the electrode and solving the severe polarization problem of ST73. Second, TiO_2 (one third of the host) provides a polar surface with an affinity for dissolved polysulfides (Figure 4), which is expected to retain soluble intermediates near the conductive carbon surfaces. Third, the mesoporous KB structure buffers the ~80% volume change during sulfur conversion, while TiO_2 anchoring prevents the detachment of active material, preserving electrode integrity during cycling.

As a result, SKT721 achieved the highest initial discharge capacity of 1300.89 mAh/g at 0.1 C, corresponding to 77.6% of the theoretical capacity (Figure 7a). In comparison, SK73 delivered moderate initial capacity (1205.70 mAh/g) but suffered from polysulfide leaching, ST73 showed limited initial capacity (1024.40 mAh/g) due to poor electronic accessibility to sulfur. Finally, SKT712 delivered a relatively low initial discharge capacity (1030.6 mAh/g at 0.1 C). Its KB content is only one third of the host, half that of SKT721, and its pore volume is correspondingly lower, so a fraction of the sulfur is neither held within the mesopores of the carbon nor connected to a continuous electron path.

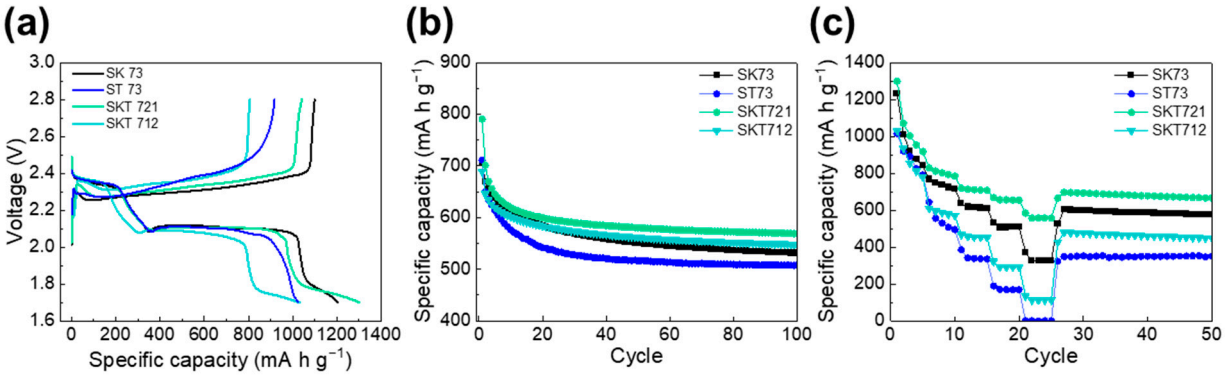


Figure 7. Electrochemical performance: (**a**) voltage profiles at 0.1 C, (**b**) cycling performance at 0.5 C, (**c**) rate capability at 0.1, 0.2, 0.5, 1, 2 C with return to 0.5 C.

Long-term cycling at 0.5 C over 100 cycles further differentiated the four compositions (Figure 7b). SK73 showed rapid capacity decay, retaining only 75.23% of its initial capacity after 100 cycles, because the weak physical confinement of KB cannot prevent progressive polysulfide dissolution and the resulting shuttle-induced loss of active material. ST73 exhibited the lowest overall retention of 71.44%. SKT712 capacity retained 84.76%, higher than SKT721 (79.52%), but from a lower initial capacity, so its absolute capacity remained below that of SKT721 throughout.

Notably, all four electrodes showed high capacity retention in the 50th–100th cycle range (SK73: 96.45%, ST73: 98.45%, SKT721: 98.63%, SKT712: 97.15%), indicating that the major capacity loss occurs predominantly during the initial cycles. The measurement does not identify the process responsible for that early loss; polysulfide dissolution, electrode reorganization and interfacial passivation would all be consistent with this observation. A high coulombic efficiency (>95%) and stable discharge capacity were sustained throughout 100 cycles.

Rate capability was evaluated at 0.1, 0.2, 0.5, 1.0 and 2.0 C, with five cycles at each step, followed by a return to 0.5 C (Figure 7c). These measurements were performed on a separate set of cells from those of Figure 7b, so capacities should be compared within each figure. The compositions are separated far more sharply here than under prolonged cycling at a single rate that at 2.0 C, 3rd cycle, the discharge capacities were approximately 327.70 mAh/g (SK73), 0.48 mAh/g (ST73), 557.59 mAh/g (SKT721) and 112.21 mAh/g (SKT712).

ST73, which contains no conductive carbon in the host, delivered almost no capacity at 2.0 C, consistent with sulfur that is chemically retained but electronically isolated. SKT712, with KB at one third of the host, retained about 112.21 mAh/g at 2.0 C, well below SK73. SKT721 retained about 557.59 mAh/g, exceeding both the carbon-only and the oxide-rich compositions. Plotted against TiO_2 fraction (0, 1/3, 2/3, 1 of the host), the capacity at 2.0 C therefore passes through a maximum at SKT721: a small addition of TiO_2 to a carbon host improves high-rate performance, while a larger addition decreases properties of the carbon network and degrades electrical properties.

The results show that the KB:TiO_2 ratio governs a trade-off rather than a single trend. Among the carbon-containing composites, increasing the TiO_2 fraction improves percentage retention; SK73 75.23%, SKT721 79.52%, SKT712 84.76%. ST73 falls outside this trend at 71.44%, since with no carbon in the host, its capacity is limited by utilization rather than by retention. The two effects act in opposite directions, and the delivered capacity is therefore maximized at an intermediate composition. Both the capacity at 2.0 C and the 100th-cycle capacity at 0.5 C are highest at SKT721, identifying KB:TiO_2 = 2:1 as the optimum within the range examined. The electrochemical comparison above covers all four compositions. The following CV and ex situ XRD measurements were used to identify the reaction mechanism

behind these differences, so they were carried out on the two single-component hosts, SK73 and ST73, which define the two limiting cases, and on SKT721, which showed the best performance among the mixed hosts. SKT712 contains the same two components as SKT721 and differs only in their ratio, so it is expected to fall between these cases and was not measured again.

Cyclic voltammetry (CV) was performed at a scan rate of 0.1 mV/s within a potential window of 1.6–3.0 V (vs. Li/Li^+) for five cycles, as shown in Figure 8. The SK73 displayed the typical two-step redox behavior of liquid-to-solid phase transitions in the Li-S system (Figure 8a). During the cathodic sweep, the first reduction peak located at approximately 2.25 V corresponds to the ring-opening reduction in S_8 molecules to soluble, long-chain lithium polysulfides (Li_2S_n, $4 \leq n \leq 8$). The subsequent reduction peak situated near 2.0–2.1 V represents the further reduction in these soluble intermediates into insoluble discharge products (Li_2S_2/Li_2S), a process governed by kinetically slower solid-phase conversion [37–39]. During the reverse anodic sweep, a prominent oxidation peak emerged near 2.36 V, reflecting the conversion of the solid sulfides (Li_2S_2, Li_2S) back to sulfur. These redox peaks were sharp and well-defined, displaying good reproducibility with an overlapping profile over five cycles. The stable electrochemical signature confirms that the high electronic conductivity and mesoporous structure of KB facilitate charge-transfer kinetics and efficient electrolyte wetting at the electrode–electrolyte interfaces. In contrast, the ST73 exhibited a different CV profile (Figure 8b). The oxidation peak shifted to more anodic potentials while the reduction peaks remained nearly unchanged, resulting in a pronounced increase in peak potential separation (ΔEp) and diminished peak current densities. These features indicate larger polarization in ST73, which is consistent with the low electronic conductivity of TiO_2 ($\sigma \approx 10^{-12}$ S/cm).

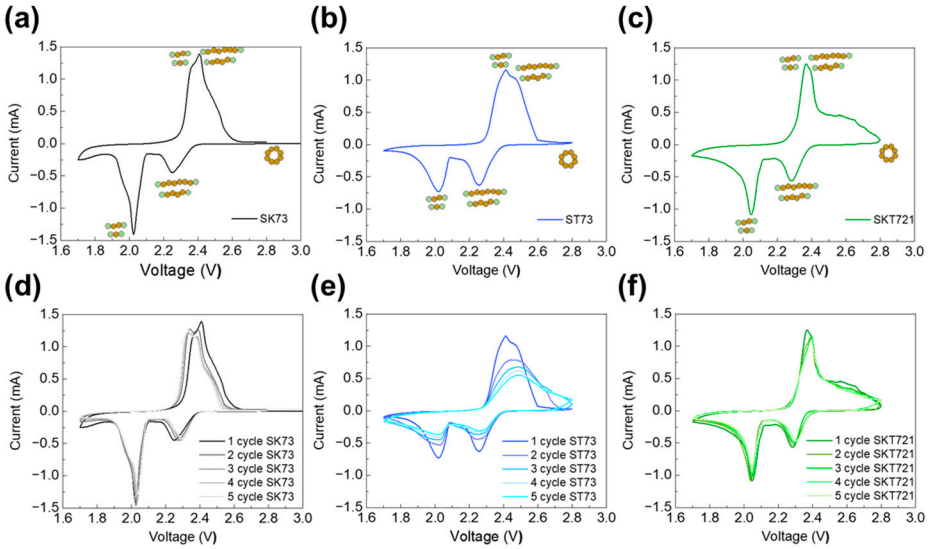


Figure 8. CV results at 0.1 mV/s: (**a**) SK73, (**b**) ST73, (**c**) SKT721; five-cycle overlays for (**d**) SK73, (**e**) ST73, (**f**) SKT721 (brown circles: sulfur, green circles: lithium).

Despite the strong Ti^{4+}–S^{2-} Lewis acid–base anchoring, the lack of conductive pathways severely compromises the electrochemical utilization of sulfur. Over repeated cycles, the redox peaks of the ST73 underwent weakening (Figure 8e), leading to the accumulation of unconverted polysulfides. A similar polarization trend was reported by Nizami et al. [27] in low-pore-volume BP800-based electrodes, highlighting that insufficient electronic pathways are a common barrier to sulfur utilization. These results show that an oxide-only host, while favorable for chemical polysulfide retention, fails to guarantee efficient charge transfer.

The CV profile of the SKT721 (Figure 8c) showed redox behavior intermediate between that of SK73 and ST73. Both cathodic and anodic peaks emerged at potentials close to those of SK73, indicating that the conductive KB network in SKT721 keeps the redox reactions kinetically close to those of the carbon-only host. The peak potential separation (ΔEp), measured between the second reduction peak and the oxidation peak, was 320 mV for SKT721, 330 mV for SK73 and 390 mV for ST73. The peak currents followed the same order: the second reduction peak reached −1.42 mA for SK73 and −1.11 mA for SKT721, but only −0.73 mA for ST73. Adding TiO_2 at a KB:TiO_2 ratio of 2:1 therefore does not measurably increase the polarization relative to the carbon-only host, while the oxide-only host shows both the largest separation and the weakest peak currents.

Moreover, the five-cycle overlay of SKT721 (Figure 8f) showed excellent reproducibility with minimal peak shift. This reversible behavior indicates that the TiO_2-mediated polysulfide anchoring stabilizes the redox reactions, thereby suppressing the progressive degradation observed in SK73 over extended cycles relatively.

The CV analysis reveals a clear trade-off between SK73 (fast kinetics but weak polysulfide trapping) and ST73 (strong polysulfide trapping but poor kinetics). This trade-off provides the basis for the dual-confinement design. KB provides a continuous electronic conduction network and a mesoporous structure that maximizes initial sulfur utilization, but its nonpolar surface interacts with polysulfides only through weak physisorption-type forces, substantially weaker than the chemical interactions available on a polar oxide surface, so active material is gradually lost during cycling [25,26,28]. Although TiO_2 forms strong chemical bonds with polysulfides through Ti^{4+}–S^{2-} Lewis acid–base interactions [28,32], suppressing the shuttle effect, its wide bandgap (~3.2 eV) causes large overpotential and limits redox efficiency.

X-ray diffraction (XRD) analysis was performed to elucidate the crystalline state of sulfur and verify the structural integrity of the host materials, as illustrated in Figure 9. The XRD pattern of the SK73 showed well-defined reflection peaks corresponding to orthorhombic elemental sulfur (S_8; JCPDS No. 08-0247) at 2θ = 23.1°, 25.8°, and 27.7°. This feature indicates that a portion of the melt-diffused sulfur remains crystalline within the relatively large mesopores of the KB matrix. For the ST73, the characteristic peaks of anatase TiO_2 (JCPDS No. 21-1272) appeared at 2θ = 25.3° (101), 37.8° (004), 48.0° (200), and 53.9° (105) alongside the sulfur peaks. This co-existence confirms that the anatase phase remains structurally unaltered throughout the autoclave-assisted thermal process (180 °C, 6 h). Concurrently, the SKT721 dual-confinement architecture manifested diffraction peaks originating from both crystalline sulfur and anatase TiO_2. Notably, however, the relative intensity of the sulfur peaks was suppressed compared to those of the SK73, suggesting a finer, better-dispersed sulfur distribution within the dual-host network. The persistence of crystalline sulfur peaks in KB-based samples is attributed to the relatively large mesopore dimensions of the KB framework, which facilitate partial crystallization of sulfur—a phenomenon in agreement with the previous literature reported by Nizami et al. [27].

To follow the crystalline phases through the first discharge, ex situ XRD measurements were performed on fresh and one-cycle discharged electrodes (Figure 10). After discharge, the crystalline S_8 peaks decreased in all three compositions, confirming the electrochemical conversion of sulfur. However, important differences were observed among the three samples.

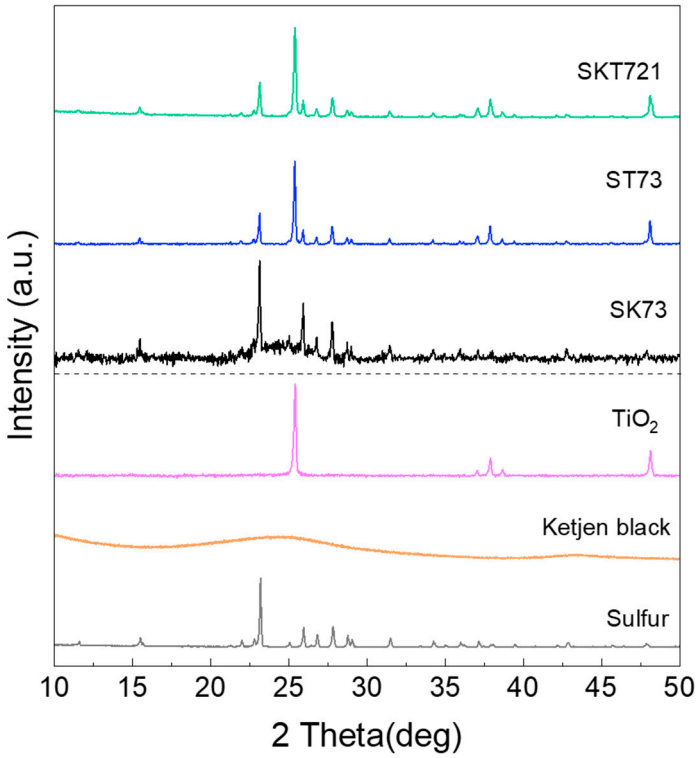


Figure 9. XRD results of materials (sulfur, Ketjen black, TiO_2) and composites (SK73, ST73, SKT721).

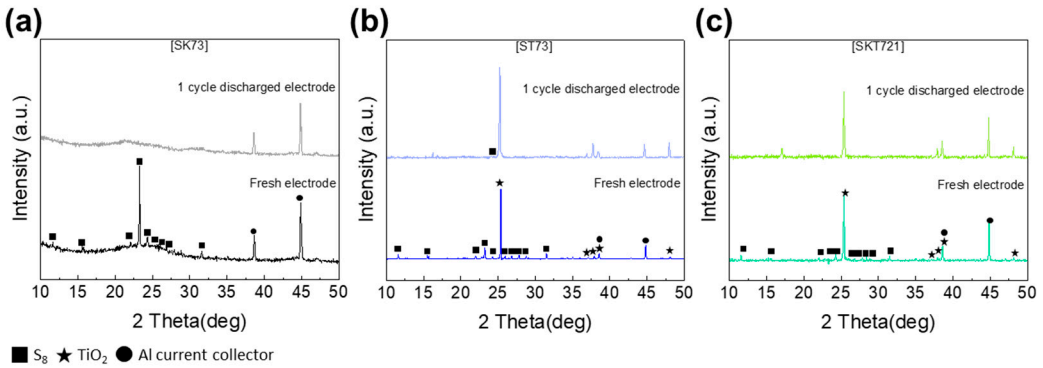


Figure 10. XRD patterns of fresh electrodes and one cycle discharged electrodes for (**a**) SK73, (**b**) ST73, and (**c**) SKT721.

In SK73, the crystalline S8 peaks were substantially reduced and the amorphous background increased, indicating effective sulfur conversion enabled by the conductive KB network. However, no crystalline Li_2S peaks were detected. The absence of crystalline Li_2S is consistent with an amorphous discharge product within the nanosized KB mesopores [40], and XRD alone cannot exclude that part of the soluble intermediates was lost to the electrolyte before conversion. In ST73, the TiO_2 anatase peaks remained unchanged after discharge, confirming the structural stability of TiO_2 during cycling. Notably, weak but identifiable residual S_8 peaks were still observed in the discharged ST73 electrode, suggesting that a portion of sulfur remained electrochemically unconverted. This incomplete conversion is due to the very low electronic conductivity of TiO_2 ($\sigma \approx 10^{-12}$ S/cm), which creates electrically isolated sulfur regions that cannot participate in electrochemical reactions, even though TiO_2 chemically binds polysulfides [41]. This result shows that chemical anchoring alone, without sufficient electronic conductivity, is not enough for full sulfur utilization. SKT721 shows a distinct post-discharge XRD pattern. The crystalline sulfur peaks nearly disappeared, indicating a conversion extent comparable to or greater

than that of SK73. The TiO_2 anatase peaks remained intact. As in SK73, no crystalline Li_2S peaks were observed, which is attributed to the amorphous state of the discharge product in the nanosized pore structure. Unlike SK73, however, SKT721 retains the anatase phase after discharge and therefore still presents a polar oxide surface, although the diffraction data cannot detect adsorbed polysulfide species and do not establish that such adsorption occurs. SKT721 retained 79.52% of its capacity after 100 cycles at 0.5 C, compared with 75.23% for SK73.

The ex situ XRD results indicate that KB and TiO_2 contribute in different ways. The KB provides the electron pathways needed for extensive sulfur conversion, which ST73 lacks. TiO_2 remains structurally intact throughout discharge and is therefore available as a polar surface for polysulfide adsorption, although diffraction cannot detect the adsorbed species themselves. In SKT721, near-complete consumption of crystalline S_8 is combined with retention of the anatase phase, so this composition attains a conversion extent comparable to that of the carbon-only host while retaining the polar component that SK73 lacks. These results provide structural support for the view that the high capacity and stable cycling of SKT721 come from the combined action of KB and TiO_2.

4. Conclusions

In this work, we designed and evaluated a dual-confinement cathode combining KB and TiO_2 to address the key challenges of Li-S batteries: the insulating nature of sulfur and the polysulfide shuttle effect. Both sulfur and TiO_2 are earth-abundant, low-cost, and non-toxic, and the resulting cathode therefore avoids the critical raw materials required by conventional transition metal oxide chemistries.

Sulfur composites with 70 wt% sulfur loading were successfully synthesized via an autoclave-based melt-diffusion process. TGA confirmed a consistent sulfur content of approximately 70 wt% across all four composites, and XRD confirmed that crystalline sulfur and anatase TiO_2 coexist in the mixed hosts. A static adsorption test with UV-vis detection showed that nano-TiO_2 removes substantially more Li_2S_6 from solution than KB at equal mass, despite a surface area roughly five times smaller, indicating that the oxide binds dissolved polysulfides through an interaction unavailable on the nonpolar carbon surface. SEM showed TiO_2 aggregates in ST73 and SKT712 but none comparable in SKT721, indicating a more even distribution of the oxide at the micrometer scale accessible with the table-top instrument used here; the nanoscale distribution of TiO_2 within the KB matrix was not verified. CV analysis showed that ST73 has the largest peak potential separation and the weakest peak currents, consistent with the low electronic conductivity of TiO_2, whereas SK73 and SKT721 lie close to each other in both respects.

SKT721 delivered the highest initial discharge capacity of 1300.89 mAh/g at 0.1 C (~77.6% of theoretical capacity) and the most stable capacity retention performance 50th–100th cycles at 0.5 C. The SKT721 combined the fast kinetics of SK73 with improved cycling stability. Ex situ XRD of discharged electrodes showed that ST73 still contains unconverted sulfur due to poor electronic conductivity, whereas SK73 converts most of sulfur but shows the largest capacity decay to 50th–100th cycle, consistent with loss of soluble intermediates. SKT721 achieves near-complete sulfur conversion while TiO_2 keeps its crystal structure. These results indicate that electronic conductivity and chemical anchoring are complementary and must be balanced.

The KB:TiO_2 ratio of 2:1 gives the best balance between sulfur utilization and capacity retention among the composite sample. This composition guideline serves as a practical foundation for cathode design in high-energy Li-S battery systems and is broadly applicable to other polar functional materials combined with conductive carbon hosts.

Author Contributions: J.S. (Jeonghwan Song): data curation, conceptualization, investigation, formal analysis, visualization and writing—original draft. J.S. (Jinju Song): supervision, funding acquisition, data curation, conceptualization, investigation and writing—review & editing. I.-C.J.: supervision, data curation, conceptualization. All authors have read and agreed to the published version of the manuscript.

Funding: This research was supported by the Korea Institute of Energy Technology Evaluation and Planning (KETEP) and the Ministry of Trade, Industry & Energy (MOTIE) of the Republic of Korea (Nos. RS-2022-KP002721 and RS-2024-00422151), and the Korea Institute of Energy Research (KIER-C5-8621).

Data Availability Statement: The data that support the findings of this study are available from the corresponding authors on reasonable request.

Conflicts of Interest: The authors declare no conflicts of interest.

Abbreviations

The following abbreviations are used in this manuscript:

Li-S	Lithium–sulfur
KB	Ketjen black
TiO_2	Titanium dioxide
SK73	Sulfur:Ketjen black = 7:3 composite sample
ST73	Sulfur:titanium dioxide = 7:3 composite sample
SKT712	Sulfur:Ketjen black:titanium dioxide = 7:1:2 composite sample
SKT721	Sulfur:Ketjen black:titanium dioxide = 7:2:1 composite sample
XRD	X-ray diffraction
BET	Brunauer–Emmett–Teller
TGA	Thermogravimetric analysis
SEM	Scanning electron microscopy
CV	Cyclic voltammetry

References

1. Yin, Y.-X.; Xin, S.; Guo, Y.-G.; Wan, L.-J. Lithium-Sulfur Batteries: Electrochemistry, Materials, and Prospects. *Angew. Chem. Int. Ed.* **2013**, *52*, 13186–13200. [CrossRef] [PubMed]
2. Manthiram, A.; Fu, Y.; Su, Y.-S. Challenges and Prospects of Lithium-Sulfur Batteries. *Acc. Chem. Res.* **2013**, *46*, 1125–1134. [CrossRef] [PubMed]
3. Goodenough, J.B.; Park, K.-S. The Li-Ion Rechargeable Battery: A Perspective. *J. Am. Chem. Soc.* **2013**, *135*, 1167–1176. [CrossRef] [PubMed]
4. Armand, M.; Tarascon, J.-M. Building Better Batteries. *Nature* **2008**, *451*, 652–657. [CrossRef] [PubMed]
5. IEA. Global EV Outlook 2024. Available online: https://www.iea.org/reports/global-ev-outlook-2024 (accessed on 3 August 2026).
6. Bruce, P.G.; Freunberger, S.A.; Hardwick, L.J.; Tarascon, J.-M. Li-O_2 and Li-S batteries with high energy storage. *Nat. Mater.* **2012**, *11*, 19–29. [CrossRef] [PubMed]
7. Manthiram, A.; Fu, Y.; Chung, S.-H.; Zu, C.; Su, Y.-S. Rechargeable Lithium-Sulfur Batteries. *Chem. Rev.* **2014**, *114*, 11751–11787. [CrossRef] [PubMed]
8. Seh, Z.W.; Sun, Y.; Zhang, Q.; Cui, Y. Designing high-energy lithium-sulfur batteries. *Chem. Soc. Rev.* **2016**, *45*, 5605–5634. [CrossRef] [PubMed]
9. Ji, X.; Nazar, L.F. Advances in Li-S batteries. *J. Mater. Chem.* **2010**, *20*, 9821–9826. [CrossRef]
10. Yang, Y.; Zheng, G.; Cui, Y. Nanostructured sulfur cathodes. *Chem. Soc. Rev.* **2013**, *42*, 3018–3032. [CrossRef] [PubMed]
11. Evers, S.; Nazar, L.F. New Approaches for High Energy Density Lithium-Sulfur Battery Cathodes. *Acc. Chem. Res.* **2013**, *46*, 1135–1143. [CrossRef] [PubMed]
12. Xu, R.; Lu, J.; Amine, K. Progress in Mechanistic Understanding and Characterization Techniques of Li–S Batteries. *Adv. Energy Mater.* **2015**, *5*, 1500408. [CrossRef]
13. Peng, H.-J.; Huang, J.-Q.; Cheng, X.-B.; Zhang, Q. Review on High-Loading and High-Energy Lithium-Sulfur Batteries. *Adv. Energy Mater.* **2017**, *7*, 1700260. [CrossRef]

14. Zhou, L.; Danilov, D.L.; Eichel, R.-A.; Notten, P.H.L. Host Materials Anchoring Polysulfides in Li-S Batteries Reviewed. *Adv. Energy Mater.* **2021**, *11*, 2001304. [CrossRef]
15. Mikhaylik, Y.V.; Akridge, J.R. Polysulfide Shuttle Study in the Li/S Battery System. *J. Electrochem. Soc.* **2004**, *151*, A1969–A1976. [CrossRef]
16. Li, G.; Wang, S.; Zhang, Y.; Li, M.; Chen, Z.; Lu, J. Revisiting the Role of Polysulfides in Lithium-Sulfur Batteries. *Adv. Mater.* **2018**, *30*, 1705590. [CrossRef] [PubMed]
17. Aurbach, D.; Pollak, E.; Elazari, R.; Salitra, G.; Kelley, C.S.; Affinito, J. On the Surface Chemical Aspects of Very High Energy Density, Rechargeable Li-Sulfur Batteries. *J. Electrochem. Soc.* **2009**, *156*, A694–A702. [CrossRef]
18. Li, W.; Yao, H.; Yan, K.; Zheng, G.; Liang, Z.; Chiang, Y.-M.; Cui, Y. The synergetic effect of lithium polysulfide and lithium nitrate to prevent lithium dendrite growth. *Nat. Commun.* **2015**, *6*, 7436. [CrossRef] [PubMed]
19. Ji, X.; Lee, K.T.; Nazar, L.F. A highly ordered nanostructured carbon-sulphur cathode for lithium-sulphur batteries. *Nat. Mater.* **2009**, *8*, 500–506. [CrossRef] [PubMed]
20. Zheng, G.; Yang, Y.; Cha, J.J.; Hong, S.S.; Cui, Y. Hollow Carbon Nanofiber-Encapsulated Sulfur Cathodes for High Specific Capacity Rechargeable Lithium Batteries. *Nano Lett.* **2011**, *11*, 4462–4467. [CrossRef] [PubMed]
21. Jayaprakash, N.; Shen, J.; Moganty, S.S.; Corona, A.; Archer, L.A. Porous Hollow Carbon@Sulfur Composites for High-Power Lithium-Sulfur Batteries. *Angew. Chem. Int. Ed.* **2011**, *50*, 5904–5908. [CrossRef] [PubMed]
22. Liang, C.; Dudney, N.J.; Howe, J.Y. Hierarchically Structured Sulfur/Carbon Nanocomposite Material for High-Energy Lithium Battery. *Chem. Mater.* **2009**, *21*, 4724–4730. [CrossRef]
23. Zhang, B.; Qin, X.; Li, G.R.; Gao, X.P. Enhancement of long stability of sulfur cathode by encapsulating sulfur into micropores of carbon spheres. *Energy Environ. Sci.* **2010**, *3*, 1531–1537. [CrossRef]
24. Ye, H.; Yin, Y.-X.; Xin, S.; Guo, Y.-G. Tuning the porous structure of carbon hosts for loading sulfur toward long lifespan cathode materials for Li-S batteries. *J. Mater. Chem. A* **2013**, *1*, 6602–6608. [CrossRef]
25. Pang, Q.; Liang, X.; Kwok, C.Y.; Nazar, L.F. Advances in lithium-sulfur batteries based on multifunctional cathodes and electrolytes. *Nat. Energy* **2016**, *1*, 16132. [CrossRef]
26. Liang, X.; Hart, C.; Pang, Q.; Garsuch, A.; Weiss, T.; Nazar, L.F. A highly efficient polysulfide mediator for lithium-sulfur batteries. *Nat. Commun.* **2015**, *6*, 5682. [CrossRef] [PubMed]
27. Nizami, A.; Yang, Z.; Jahangir, M.N.; Leonidakis, Z.; Zaghib, K.; Peslherbe, G.H.; Li, X. Tailoring Micro- and Mesoporosity in Carbon–Sulfur Cathodes for Improved Lithium–Sulfur Battery Performance. *Batteries* **2026**, *12*, 100. [CrossRef]
28. Seh, Z.W.; Li, W.; Cha, J.J.; Zheng, G.; Yang, Y.; McDowell, M.T.; Hsu, P.-C.; Cui, Y. Sulphur-TiO2 yolk-shell nanoarchitecture with internal void space for long-cycle lithium-sulphur batteries. *Nat. Commun.* **2013**, *4*, 1331. [CrossRef] [PubMed]
29. Pang, Q.; Kundu, D.; Nazar, L.F. A graphene-like metallic cathode host for long-life and high-loading lithium-sulfur batteries. *Mater. Horiz.* **2016**, *3*, 130–136. [CrossRef]
30. Yuan, Z.; Peng, H.-J.; Hou, T.-Z.; Huang, J.-Q.; Chen, C.-M.; Wang, D.-W.; Cheng, X.-B.; Wei, F.; Zhang, Q. Powering Lithium-Sulfur Battery Performance by Propelling Polysulfide Redox at Sulfiphilic Hosts. *Nano Lett.* **2016**, *16*, 519–527. [CrossRef] [PubMed]
31. Lei, T.; Chen, W.; Huang, J.; Yan, C.; Sun, H.; Wang, C.; Zhang, W.; Li, Y.; Xiong, J. Multi-functional Layered WS2 Nanosheets for Enhancing the Performance of Lithium-Sulfur Batteries. *Adv. Energy Mater.* **2017**, *7*, 1601843. [CrossRef]
32. Tao, X.; Wang, J.; Liu, C.; Wang, H.; Yao, H.; Zheng, G.; Seh, Z.W.; Cai, Q.; Li, W.; Zhou, G.; et al. Balancing surface adsorption and diffusion of lithium-polysulfides on nonconductive oxides for lithium-sulfur battery design. *Nat. Commun.* **2016**, *7*, 11203. [CrossRef] [PubMed]
33. Liang, X.; Garsuch, A.; Nazar, L.F. Sulfur Cathodes Based on Conductive MXene Nanosheets for High-Performance Lithium-Sulfur Batteries. *Angew. Chem. Int. Ed.* **2015**, *54*, 3907–3911. [CrossRef] [PubMed]
34. Diebold, U. The surface science of titanium dioxide. *Surf. Sci. Rep.* **2003**, *48*, 53–229. [CrossRef]
35. Thommes, M.; Kaneko, K.; Neimark, A.V.; Olivier, J.P.; Rodriguez-Reinoso, F.; Rouquerol, J.; Sing, K.S.W. Physisorption of Gases, with Special Reference to the Evaluation of Surface Area and Pore Size Distribution (IUPAC Technical Report). *Pure Appl. Chem.* **2015**, *87*, 1051–1069. [CrossRef]
36. Zaki, M.I.; Fouad, N.E.; Mekhemer, G.A.H.; Jagadale, T.C.; Ogale, S.B. TiO_2 Nanoparticle Size Dependence of Porosity, Adsorption and Catalytic Activity. *Colloids Surf. A* **2011**, *385*, 195–200. [CrossRef]
37. Elgrishi, N.; Rountree, K.J.; McCarthy, B.D.; Rountree, E.S.; Eisenhart, T.T.; Dempsey, J.L. A Practical Beginner's Guide to Cyclic Voltammetry. *J. Chem. Educ.* **2018**, *95*, 197–206. [CrossRef]
38. Huang, X.; Wang, Z.; Knibbe, R.; Luo, B.; Ahad, S.A.; Sun, D.; Wang, L. Cyclic Voltammetry in Lithium–Sulfur Batteries—Challenges and Opportunities. *Energy Technol.* **2019**, *7*, 1801001. [CrossRef]
39. Kim, S.C.; Gao, X.; Liao, S.-L.; Su, H.; Chen, Y.; Zhang, W.; Greenburg, L.C.; Pan, J.-A.; Zheng, X.; Ye, Y.; et al. Solvation-property relationship of lithium-sulphur battery electrolytes. *Nat. Commun.* **2024**, *15*, 1268. [CrossRef] [PubMed]

40. Yeon, J.-T.; Jang, J.-Y.; Han, J.-G.; Cho, J.; Lee, K.T.; Choi, N.-S. Raman Spectroscopic and X-ray Diffraction Studies of Sulfur Composite Electrodes during Discharge and Charge. *J. Electrochem. Soc.* **2012**, *159*, A1308–A1314. [CrossRef]
41. Tao, X.; Wang, J.; Ying, Z.; Cai, Q.; Zheng, G.; Gan, Y.; Huang, H.; Xia, Y.; Liang, C.; Zhang, W.; et al. Strong Sulfur Binding with Conducting Magnéli-Phase TinO2n−1 Nanomaterials for Improving Lithium–Sulfur Batteries. *Nano Lett.* **2014**, *14*, 5288–5294. [CrossRef] [PubMed]

Disclaimer/Publisher's Note: The statements, opinions and data contained in all publications are solely those of the individual author(s) and contributor(s) and not of MDPI and/or the editor(s). MDPI and/or the editor(s) disclaim responsibility for any injury to people or property resulting from any ideas, methods, instructions or products referred to in the content.